

Experimental Demonstration of Stationary Dark-State Polaritons Dressed by Dipole-Dipole Interaction

Bongjune Kim,^{1,*} and Ko-Tang Chen,¹ Kuei-You Chen,¹ Yi-Hsin Chen,^{2,3} and Ite A. Yu^{1,3,†}

¹*Department of Physics, National Tsing Hua University, Hsinchu 30013, Taiwan*

²*Department of Physics, National Sun Yat-sen University, Kaohsiung 80424, Taiwan*

³*Center for Quantum Technology, Hsinchu 30013, Taiwan*

Dark-state polaritons (DSPs) based on the effect of electromagnetically induced transparency are bosonic quasiparticles, representing the superpositions of photons and atomic ground-state coherences. It has been proposed that stationary DSPs are governed by the equation of motion closely similar to the Schrödinger equation and can be employed to achieve Bose-Einstein condensation (BEC) with transition temperature orders of magnitude higher than that of the atomic BEC. The stationary-DSP BEC is a three-dimensional system and has a far longer lifetime than the exciton-polariton BEC. In this work, we experimentally demonstrated the stationary DSP dressed by the Rydberg-state dipole-dipole interaction (DDI). The DDI-induced phase shift of the stationary DSP was systematically studied. Notably, the experimental data are consistent with the theoretical predictions. The phase shift can be viewed as a consequence of elastic collisions. In terms of thermalization to achieve BEC, the μm^2 -size interaction cross-section of the DDI can produce a sufficient elastic collision rate for the stationary DSPs. This work makes a substantial advancement toward the realization of the stationary-DSP BEC.

Diluted atomic gases were the first successful physical systems to reach the Bose-Einstein condensation (BEC) by cooling the bosonic atoms below the transition temperatures [1, 2]. In such systems, particle-particle interactions are usually weak, or their scattering lengths are typically much less than mean particle spacings—that is the diluteness. The rapid development of optical microcavities makes it possible to realize exciton-polariton BEC in solid-state systems [3–7]. Polaritons are bosonic quasiparticles resulting from photons strongly coupled to excitons' electric dipoles. The effective mass, particle density, transition temperature, thermalization time, and lifetime of polariton BECs are orders of magnitude different from those of atomic BECs. For example, the polariton BEC (the atomic BEC) has a transition temperature of 1–300 K (below 1 μK), a particle density of 10^{10} – 10^{12} cm^{-3} (10^{13} – 10^{15} cm^{-3}), and a thermalization time of 1–100 ps (1–100 ms) [4]. Concerning the uses of Bose condensates, exciton-polariton BECs are limited to two-dimensional systems and have lifetimes comparable to or shorter than thermalization times.

A unique platform of stationary dark-state polaritons (DSPs) to achieve BEC was proposed in Ref. [8]. Compared with the exciton-polariton BEC system, the stationary-DSP BEC system is three-dimensional and has a much longer lifetime. Stationary DSPs are formed by the interaction between light fields and atoms in the Λ -type system based on the effect of electromagnetically induced transparency (EIT) [9–16]. As depicted in Fig. 1(a), the Λ -type EIT system consists of two ground states $|1\rangle$ and $|2\rangle$ and one excited state $|3\rangle$ driven by the coupling and probe fields. Each DSP represents the superposition of probe photon and atomic ground-state coherence. Fleischhauer *et al.* in Ref. [8] showed that the stationary DSPs are governed by the equation of motion

closely similar to the Schrödinger equation. They further proposed utilizing a nonlinear Kerr effect to mediate the interaction between the DSPs for thermalization to achieve BEC. However, the proposed Kerr-type interaction is typically too weak to make a sufficient elastic collision rate for thermalization. Therefore, this present work aimed to substitute the dipole-dipole interaction (DDI) between Rydberg-state atoms for the Kerr-type interaction to make the stationary-DSP BEC feasible.

Rydberg atoms possess strong DDI [17–20], leading to the applications such as quantum logic gates [21–25], single-photon sources [26–28], and strongly-correlated many-body physics [29–32]. In our earlier work, we experimentally demonstrated a many-body system of Rydberg polaritons based on the EIT effect [33], where the Rydberg polariton represents the superposition of the photon and the coherence between a Rydberg and a ground state. Slow light arising from the EIT effect greatly enhances the interaction time between light and matter, which can be a couple of μs to about 10 μs in a medium of high optical depth (OD) [11, 33–35]. In the thermalization process, the high-OD medium made the interaction time compatible with the elastic collision rate of the μm^2 -size interaction cross-section due to the DDI between Rydberg polaritons. Hence, we observed a cooling effect in the transverse direction of slowly-propagating Rydberg polaritons [33].

According to Ref. [33], one could create stationary Rydberg polaritons to achieve BEC. The formation of stationary polaritons involves the four-wave mixing (FWM) process [9–16]. The ladder-type transition scheme, which typically has a very large phase mismatch in the FWM process, is employed in the Rydberg-EIT system to form the stationary Rydberg polaritons. However, the probe and coupling fields had the typical wavelengths of 780 or

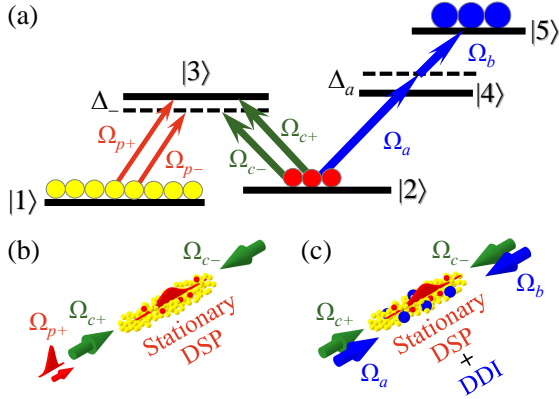


FIG. 1: (a) Relevant energy levels and laser excitations. States $|1\rangle$, $|2\rangle$, and $|3\rangle$ form the Λ -type EIT system for the creation of stationary DSPs, where $\Omega_{p\pm}$ and $\Omega_{c\pm}$ denote the Rabi frequencies of the forward/backward probe and coupling fields, respectively, and $\Delta_- = -1\Gamma$. Population oscillates between $|2\rangle$ and a Rydberg state $|5\rangle$, driven by the two-photon transition (TPT) of the fields Ω_a and Ω_b with $\Delta_a = +5\Gamma$, where $|4\rangle$ is an intermediate state of the TPT. The spontaneous decay rates of $|3\rangle$ and $|4\rangle$ are about the same and denoted as Γ ($= 2\pi \times 6$ MHz). In this work, the pair of Ω_{c+} and Ω_{p+} , that of Ω_{c-} and Ω_{p-} , and that of Ω_a and Ω_b always maintained the two-photon resonances. (b,c) Propagation directions of the laser fields in the measurements of stationary DSPs without and with the TPT or equivalently the DDI.

795 nm and around 480 nm in a Rydberg-EIT system, resulting in an FWM phase mismatch of 10^4 – 10^5 rad. Such a large phase mismatch completely destroys stationary Rydberg polaritons and makes the search for the Rydberg-polariton BEC impractical.

In this study, we proposed and experimentally demonstrated the stationary DSPs possessing the Rydberg-state DDI. In addition to the probe and coupling fields that formed the stationary DSP via the FWM process, two more laser fields were applied to drive the two-photon transition (TPT) of $|2\rangle \rightarrow |4\rangle \rightarrow |5\rangle$ as shown by Fig. 1(a). The TPT generated the Rabi oscillation between the population of the ground state $|2\rangle$ and that of the Rydberg state $|5\rangle$, as well as between the ground-state coherence ρ_{21} and the Rydberg coherence ρ_{51} . Due to the existence of the Rydberg population, the DDI resulted in the phase shift and attenuation of the stationary DSP. Furthermore, we systematically measured the DDI-induced attenuation coefficient and phase shift of the stationary DSP as functions of the DDI strength. The measured data are consistent with the theoretical predictions, verifying the creation of the stationary DSP dressed by the DDI. With regard to the thermalization of stationary DSPs, the DDI can lead to a far larger elastic collision rate than the Kerr-type interaction. Hence, this work makes a substantial advancement toward the realization of the stationary-DSP BEC.

We carried out the experiment in laser-cooled ^{87}Rb

atoms with a temperature of about 350 μK . Before each measurement, the magnetic and laser fields for the production of the cold atoms were switched off, and we optically pumped all the population to a single Zeeman state. Details of the atom cloud and the experimental procedure before the measurements can be found in Refs. [33, 36].

All the laser fields had the σ_+ polarization in the experiment. In the Λ -type EIT system shown by Fig. 1(a), $|1\rangle$, $|2\rangle$, and $|3\rangle$ are $|5S_{1/2}, F=1, m_F=1\rangle$, $|5S_{1/2}, F=2, m_F=1\rangle$, and $|5P_{3/2}, F=2, m_F=2\rangle$. The EIT or probe-coupling Raman transition was driven resonantly, while the fields in the forward direction (Ω_{p+} and Ω_{c+}) had nearly zero one-photon detuning, and those in the backward direction (Ω_{p-} and Ω_{c-}) had the one-photon detuning Δ_- of -1Γ [10]. In the TPT system shown by Fig. 1(a), $|4\rangle$ is $|5P_{3/2}, F=3, m_F=2\rangle$ and $|5\rangle$ is $|32D_{5/2}, m_J=3/2 \text{ \& } 5/2\rangle$. We made the TPT resonant at nearly no DDI and set the one-photon detuning Δ_a to $+5\Gamma$ to make excitation to $|4\rangle$ negligible.

The propagation direction of Ω_{c-} was exactly opposite to that of Ω_{c+} as depicted in Fig. 1(b). When interacting with the atoms, Ω_{c+} and Ω_{p+} propagated in the nearly same direction with an angle separation of about 0.3° [10]. This angle separation ensures the phase match condition for the generation of stationary DSPs. Driving the transitions of $|2\rangle \rightarrow |4\rangle$ and $|4\rangle \rightarrow |5\rangle$, the TPT fields of Ω_a and Ω_b counterpropagated in the forward and backward directions as depicted in Fig. 1(c). The laser beams of Ω_a and Ω_b completely covered the region of stationary DSPs. Other details of the experimental setup can be found in Sec. I of the Supplemental Material (SM).

We made theoretical predictions using the optical Bloch equations of the density-matrix operator and the Maxwell-Schrödinger equations of the probe fields. Details of the equations and calculation can be found in Sec. II of the SM. The equations for the stationary DSP are very similar to those in our works of Refs. [10, 11]. The equations involving the DDI are very similar to those in our works of Refs. [33, 37], which were derived based on the mean field model [38]. In these works, the predictions are in good agreement with the experimental data.

We set $\delta_\Lambda = 0$ in the experiment, where δ_Λ is the two-photon detuning in the Λ -type EIT system. In Ref. [39], Tebben *et al.* theoretically studied a similar transition scheme, except that the TPT is replaced by a one-photon transition. They showed that the optimum δ_Λ , which maximizes the stationary-DSP energy, is equal to a half of the Rabi frequency of the one-photon transition [40]. In our TPT case, $\delta_\Lambda = 0$ is the optimum value.

Representative data that demonstrate the formation of the stationary DSP in the Λ -type EIT system are shown by Fig. 2(a). We illustrate the experimental procedure in the followings [10]: The probe pulse was sent into the atom cloud in the forward direction under the presence of only Ω_{c+} ($= 0.54\Gamma$). As the majority of the probe pulse had entered the atom cloud and propagated slowly, we

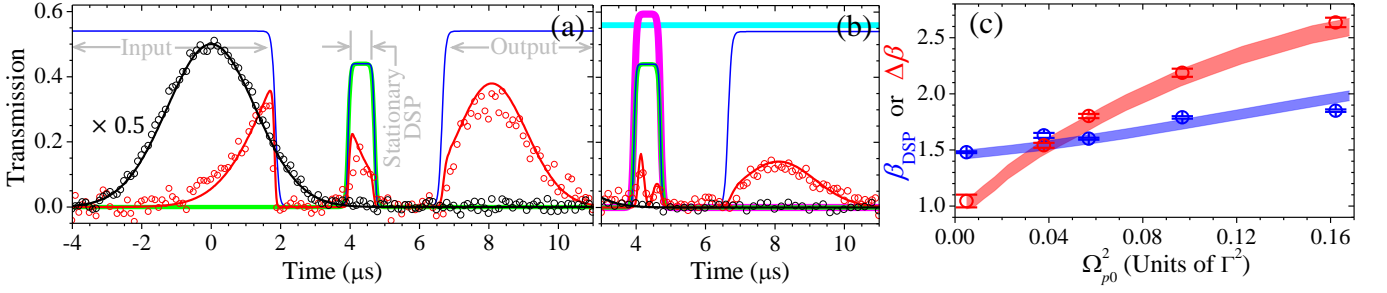


FIG. 2: (a, b) Representative experimental data of the probe pulses as functions of time without and with the TPT, respectively, and theoretical predictions. Black and red circles are the data of the input and output probe pulses in the forward direction. Black line is the Gaussian best fit of the input probe pulse, and red lines are the predictions of the output probe pulses. Blue, green, magenta, and cyan lines represent the timing sequences of the forward and backward coupling fields Ω_{c+} and Ω_{c-} and the TPT fields Ω_a and Ω_b . We do not plot the data before $t < 3 \mu\text{s}$ in (b), which are the same as those in (a). The peak Rabi frequency of the input probe pulse, Ω_{p0} , is 0.07Γ . The experimental parameters of the stationary DSP are α (optical depth) = 36, $\Omega_{c+} = 0.54\Gamma$ during the input and output stages, $\Omega_{c+} = \Omega_{c-} = 0.44\Gamma$ during the stationary DSP, γ_Λ (the ground-state decoherence rate) = $9 \times 10^{-4}\Gamma$, and $L\Delta_k$ (the degree of phase mismatch) = 0.90 rad; those of the TPT and DDI are $\Omega_a = 2.0\Gamma$, $\Omega_b = 1.6\Gamma$, γ_R (the Rydberg-state decoherence rate) = 0.020Γ , and A (the DDI coefficient) = 0.60Γ . (c) The attenuation coefficient (i.e., the logarithm of the ratio of input to output probe energies) without the TPT, β_{DSP} , and the difference between the attenuation coefficients with and without the TPT, $\Delta\beta$ ($\equiv \beta_{\text{DSP+DDI}} - \beta_{\text{DSP}}$), as functions of Ω_{p0}^2 . Blue and red circles are the data of β_{DSP} and $\Delta\beta$, respectively. Based on the above-mentioned parameters, blue and red areas are the predictions with the uncertainties due to the fluctuation of ± 1 in α and that of $\pm 1 \times 10^{-4}\Gamma$ in γ_Λ .

quickly switched off Ω_{c+} as indicated by the falling edge of the blue line at $t \approx 2 \mu\text{s}$. At this moment, the part of the pulse centering around its peak inside the cloud was stored. The black circles after $t \approx 2 \mu\text{s}$ and the red circles before $t \approx 2 \mu\text{s}$ were the parts of the pulse outside the cloud, and they were not stored. After a fixed storage time, we simultaneously switched on Ω_{c+} and Ω_{c-} (both are equal to 0.44Γ) to form the stationary DSP for a duration of about $0.7 \mu\text{s}$, as indicated by the green and blue pulses. Within the stationary-DSP duration, the leakage of the probe pulse in the forward direction is shown by the red circles underneath the blue square pulse. There was also the leakage in the backward direction, but we did not detect it. After the stationary-DSP duration, we turned off Ω_{c+} and Ω_{c-} and stored the remaining probe pulse for another fixed storage time. Finally, we switched on Ω_{c+} ($= 0.54\Gamma$) again and retrieved the probe pulse. The red circles after the rising edge of the blue line at $t \approx 6.5 \mu\text{s}$ represent the retrieved probe pulse.

The TPT fields Ω_a ($= 2.0\Gamma$) and Ω_b ($= 1.6\Gamma$) were applied to induce the DDI during the stationary DSP. Since the pulse width of Ω_b did not affect the results, Ω_b was constantly present. Figure 2(b) shows the representative data of the stationary DSP dressed by the DDI, and the magenta square pulse corresponds to the TPT duration. The TPT fields produced the Rabi oscillation between $|2\rangle$ and $|5\rangle$. Consequently, in the figure the red circles of the probe leakage within the duration exhibit the oscillation. We were able to find the TPT resonance by maximizing the oscillation amplitude. The node (anti-node) of the oscillation corresponds to all the population in $|5\rangle$ (in $|2\rangle$). Because of the DDI-induced attenuation, the retrieved probe energy in Fig. 2(b) is less than that

in Fig. 2(a).

In the measurements of the DSPs without and with the TPT such as Fig. 2, the Rabi frequencies Ω_{c+} , Ω_{c-} , and Ω_a , the optical density (α), and the ground-state decoherence rate (γ_Λ) were pre-determined [36, 42, 43]. Details of the determination methods and representative data are presented in Secs. I and III of the SM. The Rabi frequency Ω_b was determined by the period of the Rabi oscillation during the TPT. The stationary DSP is generated by the FWM process, in which the phase mismatch causes the energy loss [11, 44, 45]. The degree of phase mismatch is given by $L\Delta_k$ [see Eq. (S18) in the SM]. We determined the value of $L\Delta_k$ by the comparison between the experimental results and theoretical predictions. Details can be found in Sec. IV of the SM, which provides more evidence for the formation of stationary DSPs.

We varied the input probe power [46], while keeping the pulse width and beam profile the same, and measured the data similar to those in Figs. 2(a) and 2(b). The population in $|2\rangle$, ρ_{22} , is about equal to $|\Omega_{p+}/\Omega_{c+}|^2$ due to the EIT effect. Thus, a larger input probe intensity, Ω_{p0}^2 , resulted in larger ρ_{22} and ρ_{55} , which produced a higher DDI strength [33]. We determined the attenuation coefficients, β_{DSP} and $\beta_{\text{DSP+DDI}}$, as functions of Ω_{p0}^2 , where β_{DSP} and $\beta_{\text{DSP+DDI}}$ are defined as the logarithm of the ratio of input to output probe energies without and with the DDI. In Fig. 2(c), the blue and red circles represent the data of β_{DSP} and $\Delta\beta$ ($\equiv \beta_{\text{DSP+DDI}} - \beta_{\text{DSP}}$). Since the OD fluctuated about ± 1 and the ground-state decoherence rate γ_Λ fluctuated about $\pm 1 \times 10^{-4}\Gamma$, the predictions of β_{DSP} and $\Delta\beta$ are plotted as the blue and red areas.

The TPT made the population (coherence) oscillate between $|2\rangle$ and $|5\rangle$ (between ρ_{21} and ρ_{51}), and the pop-

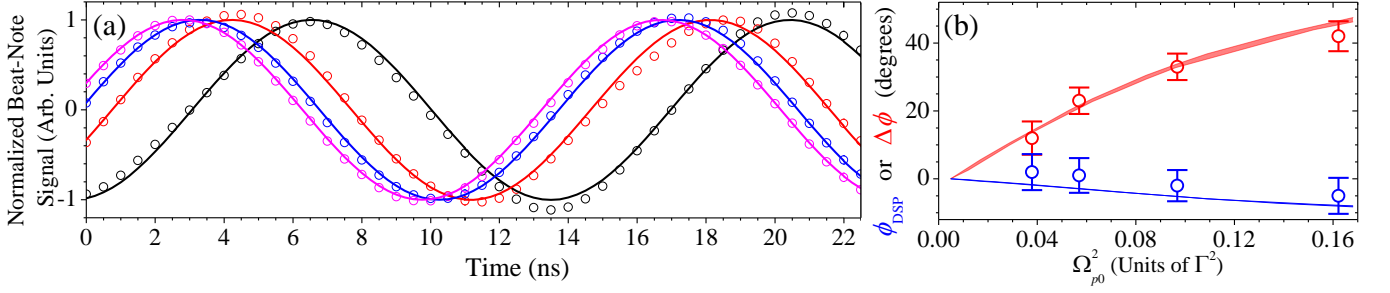


FIG. 3: (a) Representative data of normalized beat-note signals, showing phase evolutions at the peaks of the retrieved probe pulses. Circles are the experimental data and lines are their best fits. In the presence of the TPT (or equivalently the DDI) during the stationary DSP, red, blue, and magenta colors correspond to the peak Rabi frequency of the input probe, Ω_{p0} , of 0.07Γ , 0.24Γ , and 0.40Γ , respectively. There are three beat-note signals without the TPT (black color), which serve as the reference phases. We make these three signals completely overlap and plot only one here. The experimental parameters are the same as those specified in the caption of Fig. 2. Since the DDI is negligible at $\Omega_{p0} = 0.07\Gamma$, the phase difference between the red and black data is mainly the result of the Rabi oscillation. On the other hand, the phase difference of $+42^\circ$ (or $+23^\circ$) between the magenta (or blue) and red data is the consequence of the DDI. (b) Blue circles are the data of phase shift of the output probe pulse without the TPT, ϕ_{DSP} , and red circles are those of difference between the phase shifts with and without the TPT, $\Delta\phi$ ($\equiv \phi_{\text{DSP+DDI}} - \phi_{\text{DSP}}$). The phase shifts at $\Omega_{p0} = 0.07\Gamma$ are subtracted from the data. Blue and red areas are the predictions with the uncertainties due to the fluctuations of α and γ_Λ .

ulation in [5] induced the DDI. We characterized the DDI coefficient, A , which is defined as the decoherence rate (also frequency shift) per ρ_{55} [33, 37, 38]. See also Eqs. (S15) and (S16) in the SM for the definition of A . The ratio of retrieved probe energies with to without the TPT was measured against the input probe intensity or equivalently the peak Rabi frequency square, Ω_{p0}^2 , as shown in Fig. 2(c). We compared the data with the predictions to determine $A = 0.60\Gamma$ and γ_R (the Rydberg-state decoherence rate) $= 0.020\Gamma$. We also estimated the value of A , and details can be found in Sec. V of the SM. The estimation gives A of 0.54Γ , indicating that the experimentally determined A of 0.60Γ is reasonable.

The DDI induces a phase shift of the stationary DSP, and the phase of the retrieved probe pulse is shifted. To further verify the creation of the stationary DSP dressed by the DDI, we applied the TPT and measured the phase shift of the retrieved probe pulse, i.e., the difference of the phases with and without the atoms. The beat-note interferometer was employed to measure the phase evolution around the pulse peak [33, 47]. The experimental parameters in the phase measurement are the same as those in the transmission measurement. In Fig. 3(a), the black circles are the beat-note data without the TPT or DDI, which serve as the reference for the other data. The red, blue, and magenta circles represent the data with increasing values of Ω_{p0}^2 or DDI strength. A larger DDI strength resulted in a larger phase shift as expected.

To quantitatively confirm the DDI effect, we measured the phase shifts of the retrieved probe pulses without and with the TPT, ϕ_{DSP} and $\phi_{\text{DSP+DDI}}$, respectively, as functions of Ω_{p0}^2 . In Fig. 3(b), the blue and red circles represent ϕ_{DSP} and $\Delta\phi$ ($\equiv \phi_{\text{DSP+DDI}} - \phi_{\text{DSP}}$). We subtracted the measured phase shift at $\Omega_{p0} = 0.07\Gamma$ from the data.

The subtraction removes the phase shift contributed from the Rabi oscillation. Thus, $\Delta\phi$ exhibits mainly the DDI effect. More details can be found in Sec. VII of the SM. Without the DDI, ϕ_{DSP} of the stationary DSP depends on the probe intensity a little. Owing to the DDI, $\Delta\phi$ depends on the probe intensity significantly. The blue and red areas are the theoretical predictions. In the theoretical calculation, all the parameters are non-adjustable and experimentally pre-determined. The consistency between the data and predictions is satisfactory, confirming that the stationary DSP indeed possessed the DDI.

In conclusion, we experimentally demonstrated the formation of the stationary DSP dressed by the DDI, using the scheme of the Λ -type EIT system together with the TPT-driven Rabi oscillation between a ground state and a Rydberg state. The scheme overcomes the severe problem of a large phase mismatch in the direct formation of the stationary Rydberg polariton. Phase shifts of stationary DSPs can be seen as the consequence of the elastic collision, which is the key to thermalization. We measured the phase shift of the stationary DSPs or retrieved probe pulse as a function of the DDI strength. The experimental data are consistent with the theoretical predictions calculated with the parameters pre-determined by independent methods. A phase shift of 0.73 rad or 42° during a time period of about $0.7 \mu\text{s}$ has been achieved. The phase shift per unit time, i.e., an indication of the elastic collision rate, obtained in this work is comparable to that obtained in Ref. [33], showing the cooling effect in the transverse plane of moving Rydberg polaritons. As proposed in Ref. [8], the system of stationary DSPs is the possible platform for a three-dimensional and long-lifetime Bose condensate. Our work made the stationary DSPs carry the DDI and provided a feasible method of

thermalization for the realization of BEC.

ACKNOWLEDGMENTS

This work was supported by Grants No. 110-2639-M-007-001-ASP and No. 111-2639-M-007-001-ASP of the National Science and Technology Council, Taiwan. The authors thank the fruitful discussions with Prof. Gediminas Juzeliūnas and Mr. Chin-Jen Yang.

* Electronic address: upfe11@gmail.com

† Electronic address: yu@phys.nthu.edu.tw

- [1] M. H. Anderson, J. R. Ensher, M. R. Matthews, C. E. Wieman, and E. A. Cornell, “Observation of Bose-Einstein Condensation in a Dilute Atomic Vapor,” *Science* **269**, 198 (1995).
- [2] K. B. Davis, M.-O. Mewes, M. R. Andrews, N. J. van Druten, D. S. Durfee, D. M. Kurn, and W. Ketterle, “Bose-Einstein Condensation in a Gas of Sodium Atoms,” *Phys. Rev. Lett.* **75**, 3969 (1995).
- [3] J. Kasprzak, M. Richard, S. Kundermann, A. Baas, P. Jeambrun, J. M. J. Keeling, F. M. Marchetti, M. H. Szymańska, R. André, J. L. Staehli, V. Savona, P. B. Littlewood, B. Deveaud, and Le Si Dang, “Bose-Einstein condensation of exciton polaritons,” *Nature* **443**, 409 (2006).
- [4] H. Deng, H. Haug, and Y. Yamamoto, “Exciton-polariton Bose-Einstein condensation,” *Rev. Mod. Phys.* **82**, 1489 (2010).
- [5] H. Deng, D. Press, S. Götzinger, G. S. Solomon, R. Hey, K. H. Ploog, and Y. Yamamoto, “Quantum Degenerate Exciton-Polaritons in Thermal Equilibrium,” *Phys. Rev. Lett.* **97**, 146402 (2006).
- [6] Y. Sun, P. Wen, Y. Yoon, G. Liu, M. Steger, L. N. Pfeiffer, K. West, D. W. Snoke, and K. A. Nelson, “Bose-Einstein Condensation of Long-Lifetime Polaritons in Thermal Equilibrium,” *Phys. Rev. Lett.* **118**, 016602 (2017); Erratum *Phys. Rev. Lett.* **118**, 149901 (2017).
- [7] V. Y. Shishkov, E. S. Andrianov, A. V. Zasedatelev, P. G. Lagoudakis, and Y. E. Lozovik, “Exact Analytical Solution for the Density Matrix of a Nonequilibrium Polariton Bose-Einstein Condensate,” *Phys. Rev. Lett.* **128**, 065301 (2022).
- [8] M. Fleischhauer, J. Otterbach, and R. G. Unanyan, “Bose-Einstein Condensation of Stationary-Light Polaritons,” *Phys. Rev. Lett.* **101**, 163601 (2008).
- [9] M. Bajcsy, A. S. Zibrov, and M. D. Lukin, “Stationary pulses of light in an atomic medium,” *Nature* **426**, 638 (2003).
- [10] Y.-W. Lin, W.-T. Liao, T. Peters, H.-C. Chou, J.-S. Wang, H.-W. Cho, P.-C. Kuan, and I. A. Yu, “Stationary Light Pulses in Cold Atomic Media and without Bragg Gratings,” *Phys. Rev. Lett.* **102**, 213601 (2009).
- [11] Y.-H. Chen, M.-J. Lee, W. Hung, Y.-C. Chen, Y.-F. Chen, and I. A. Yu, “Demonstration of the Interaction between Two Stopped Light Pulses,” *Phys. Rev. Lett.* **108**, 173603 (2012).
- [12] F. Blatt, L. S. Simeonov, T. Halfmann, and T. Peters, “Stationary light pulses and narrowband light storage in a laser-cooled ensemble loaded into a hollow-core fiber,” *Phys. Rev. A* **94**, 043833 (2016).
- [13] G. T. Campbell, Y.-W. Cho, J. Su, J. Everett, N. Robins, P. K. Lam, and B. Buchler, “Direct imaging of slow, stored and stationary EIT polaritons,” *Quantum Sci. Technol.* **2**, 034010 (2017).
- [14] K.-K. Park, Y.-W. Cho, Y.-T. Chough, and Y.-H. Kim, “Experimental Demonstration of Quantum Stationary Light Pulses in an Atomic Ensemble,” *Phys. Rev. X* **8**, 021016 (2018).
- [15] J. L. Everett, D. B. Higginbottom, G. T. Campbell, P. K. Lam, and B. C. Buchler, “Stationary light in atomic media,” *Adv. Quantum Technol.* **2**, 1800100, (2019).
- [16] U.-S. Kim, Y. S. Ihn, C.-H. Lee, and Y.-H. Kim, “Trapping a free-propagating single-photon into an atomic ensemble as a quantum stationary light pulse,” *AVS Quantum Sci.* **4**, 021403 (2022).
- [17] M. D. Lukin, M. Fleischhauer, R. Cote, L. M. Duan, D. Jaksch, J. I. Cirac, and P. Zoller, “Dipole Blockade and Quantum Information Processing in Mesoscopic Atomic Ensembles,” *Phys. Rev. Lett.* **87**, 037901 (2001).
- [18] D. Tong, S. M. Farooqi, J. Stanojevic, S. Krishnan, Y. P. Zhang, R. Côté, E. E. Eyler, and P. L. Gould, “Local Blockade of Rydberg Excitation in an Ultracold Gas,” *Phys. Rev. Lett.* **93**, 063001 (2004).
- [19] R. Heidemann, U. Raitzsch, V. Bendkowsky, B. Butscher, R. Löw, L. Santos, and T. Pfau, “Evidence for Coherent Collective Rydberg Excitation in the Strong Blockade Regime,” *Phys. Rev. Lett.* **99**, 163601 (2007).
- [20] M. Saffman, T. G. Walker, and K. Mølmer, “Quantum information with Rydberg atoms,” *Rev. Mod. Phys.* **82**, 2313 (2010).
- [21] M. Saffman and T. G. Walker, “Analysis of a quantum logic device based on dipole-dipole interactions of optically trapped Rydberg atoms,” *Phys. Rev. A* **72**, 022347 (2005).
- [22] T. Keating, R. L. Cook, A. M. Hankin, Y.-Y. Jau, G. W. Biedermann, and I. H. Deutsch, “Robust quantum logic in neutral atoms via adiabatic Rydberg dressing,” *Phys. Rev. A* **91**, 012337 (2015).
- [23] D. Tiarks, S. Schmidt-Eberle, T. Stolz, G. Rempe, and S. Dürr, “A photon-photon quantum gate based on Rydberg interactions,” *Nat. Phys.* **15**, 124 (2019).
- [24] J. Vaneecloo, S. Garcia, and A. Ourjoumtsev, “Intracavity Rydberg Superatom for Optical Quantum Engineering: Coherent Control, Single-Shot Detection, and Optical π Phase Shift,” *Phys. Rev. X* **12**, 021034 (2022).
- [25] T. Stolz, H. Hegels, M. Winter, B. Röhr, Y.-F. Hsiao, L. Husel, G. Rempe, and S. Dürr, “Quantum-Logic Gate between Two Optical Photons with an Average Efficiency above 40%,” *Phys. Rev. X* **12**, 021035 (2022).
- [26] F. Ripka, H. Kübler, R. Löw, and T. Pfau, “A room-temperature single-photon source based on strongly interacting Rydberg atoms,” *Science* **362**, 446 (2018).
- [27] D. P. Ornelas-Huerta, A. N. Craddock, E. A. Goldschmidt, A. J. Hachtel, Y. Wang, P. Bienias, A. V. Gorshkov, S. L. Rolston, and J. V. Porto, “On-demand indistinguishable single photons from an efficient and pure source based on a Rydberg ensemble,” *Optica* **7**, 813 (2020).
- [28] S. Shi, B. Xu, K. Zhang, G.-S. Ye, D.-S. Xiang, Y. Liu, J. Wang, D. Su, and L. Li, “High-fidelity photonic quantum

- logic gate based on near-optimal Rydberg single-photon source,” *Nat. Commun.* **13**, 4454 (2022).
- [29] G. Pupillo, A. Micheli, M. Boninsegni, I. Lesanovsky, and P. Zoller, “Strongly Correlated Gases of Rydberg-Dressed Atoms: Quantum and Classical Dynamics,” *Phys. Rev. Lett.* **104**, 223002 (2010).
- [30] T. Peyronel, O. Firstenberg, Q.-Y. Liang, S. Hofferberth, A. V. Gorshkov, T. Pohl, M. D. Lukin, and V. Vuletić, “Quantum nonlinear optics with single photons enabled by strongly interacting atoms,” *Nature* **488**, 57 (2012).
- [31] M. Moos, M. Höning, R. Unanyan, and M. Fleischhauer, “Many-body physics of Rydberg dark-state polaritons in the strongly interacting regime,” *Phys. Rev. A* **92**, 053846 (2015).
- [32] A. Browaeys and T. Lahaye, “Many-body physics with individually controlled Rydberg atoms,” *Nat. Phys.* **16**, 132 (2020).
- [33] B. Kim, K.-T. Chen, S.-S. Hsiao, S.-Y. Wang, K.-B. Li, J. Ruseckas, G. Juzeliūnas, T. Kirova, M. Auzinsh, Y.-C. Chen, Y.-F. Chen, and I. A. Yu, “A weakly-interacting many-body system of Rydberg polaritons based on electromagnetically induced transparency,” *Commun. Phys.* **4**, 101 (2021).
- [34] Y.-H. Chen, M.-J. Lee, I.-C. Wang, S. Du, Y.-F. Chen, Y.-C. Chen, and I. A. Yu, “Coherent Optical Memory with High Storage Efficiency and Large Fractional Delay,” *Phys. Rev. Lett.* **110**, 083601 (2013).
- [35] Y.-S. Wang, K.-B. Li, C.-F. Chang, T.-W. Lin, J.-Q. Li, S.-S. Hsiao, J.-M. Chen, Y.-H. Lai, Y.-C. Chen, Y.-F. Chen, C.-S. Chu, and I. A. Yu, “Temporally-ultralong biphotons with a linewidth of 50 kHz,” *arXiv:2205.13778*.
- [36] B. Kim, K.-T. Chen, C.-Y. Hsu, S.-S. Hsiao, Y.-C. Tseng, C.-Y. Lee, S.-L. Liang, Y.-H. Lai, J. Ruseckas, G. Juzeliūnas, and I. A. Yu, “Effect of laser-frequency fluctuation on the decay rate of Rydberg coherence,” *Phys. Rev. A* **100**, 013815 (2019).
- [37] K.-T. Chen, B. Kim, C.-C. Su, S.-S. Hsiao, S.-J. Huang, W.-T. Liao, and I. A. Yu, “Increasing the decoherence rate of Rydberg polaritons due to accumulating dark Rydberg atoms,” *Phys. Rev. Research* **4**, 023024 (2022).
- [38] S.-S. Hsiao, K.-T. Chen, and I. A. Yu, “Mean field theory of weakly-interacting Rydberg polaritons in the EIT system based on the nearest-neighbor distribution,” *Opt. Express* **28**, 28414 (2020).
- [39] A. Tebben, C. Hainaut, A. Salzinger, T. Franz, S. Geier, G. Zürn, and M. Weidemüller, “A stationary Rydberg polariton,” *arXiv:2108.00657*.
- [40] Y.-C. Chen, Y.-A. Liao, H.-Y. Chiu, J.-J. Su, and I. A. Yu, “Observation of the quantum interference phenomenon induced by interacting dark resonances,” *Phys. Rev. A* **64**, 053806 (2001).
- [41] W.-T. Liao, T. Peters, E.-C. Shen, and I. A. Yu, “Propagation, Broadening, and Energy Decay of Quasi-Stationary Light Pulses in Thermal Atoms,” *Chin. J. Phys.* **47**, 817 (2009).
- [42] C.-Y. Wang, Y.-F. Chen, S.-C. Lin, W.-H. Lin, P.-C. Kuan, and I. A. Yu, “Low-light-level all-optical switching,” *Opt. Lett.* **31**, 2350 (2006).
- [43] Y.-F. Chen, C.-Y. Wang, S.-H. Wang, and I. A. Yu, “Low-Light-Level Cross-Phase-Modulation Based on Stored Light Pulses,” *Phys. Rev. Lett.* **96**, 043603 (2006).
- [44] D. A. Braje, V. Balić, S. Goda, G. Y. Yin, and S. E. Harris, “Frequency Mixing Using Electromagnetically Induced Transparency in Cold Atoms,” *Phys. Rev. Lett.* **93**, 183601 (2004).
- [45] K.-F. Chang, T.-P. Wang, C.-Y. Chen, Y.-H. Chen, Y.-S. Wang, Y.-F. Chen, Y.-C. Chen, and I. A. Yu, “Low-loss high-fidelity frequency beam splitter with tunable split ratio based on electromagnetically induced transparency,” *Phys. Rev. Research* **3**, 013096 (2021).
- [46] Details of the experimental data and theoretical predictions at $\Omega_{p0} \geq 0.3\Gamma$ can be found in Sec. VI of the SM.
- [47] Y.-F. Chen, Y.-C. Liu, Z.-H. Tsai, S.-H. Wang, and I. A. Yu, “Beat-note interferometer for direct phase measurement of photonic information,” *Phys. Rev. A* **72**, 033812 (2005).

SUPPLEMENTAL MATERIAL

Experimental Demonstration of Stationary Dark-State Polaritons Dressed by Dipole-Dipole Interaction

Bongjune Kim,^{1,*} and Ko-Tang Chen,¹ Kuei-You Chen,¹ Yi-Hsin Chen,^{2,3} and Ite A. Yu^{1,3†}

¹*Department of Physics, National Tsing Hua University, Hsinchu 30013, Taiwan*

²*Department of Physics, National Sun Yat-sen University, Kaohsiung 80424, Taiwan*

³*Center for Quantum Technology, Hsinchu 30013, Taiwan*

I. EXPERIMENTAL SETUP

In the system for the creation of the stationary dark-state polaritons (DSP) [1], there are two ground states $|1\rangle$ ($|5S_{1/2}, F=1, m_F=1\rangle$) and $|2\rangle$ ($|5S_{1/2}, F=2, m_F=1\rangle$) and an excited state $|3\rangle$ ($|5P_{3/2}, F=2, m_F=2\rangle$) to form the Λ -type configuration of the electromagnetically induced transparency (EIT) effect. Since laser-cooled ^{87}Rb atoms were employed in the experiment, all the energy levels are referred to those of ^{87}Rb . The coupling (or probe) fields propagated in the forward and backward directions, and their Rabi frequencies are denoted as Ω_{c+} and Ω_{c-} (or Ω_{p+} and Ω_{p-}), respectively. Both coupling fields drove the transition from $|2\rangle$ to $|3\rangle$, and both probe fields drove that from $|1\rangle$ to $|3\rangle$. All the fields had the $\sigma+$ polarization. The peak Rabi frequency of the input Gaussian probe pulse (denoted as Ω_{p0}) ranged from 0.07Γ to 0.40Γ , where Γ ($= 2\pi \times 6$ MHz) is the spontaneous decay rate of $|3\rangle$. Throughout this work, $\Omega_{c+} = 0.54\Gamma$ during the input and output stages of the probe pulse, and $\Omega_{c+} = \Omega_{c-} = 0.44\Gamma$ during the stationary DSP. The determination method of Ω_{c+} and Ω_{c-} will be described in Sec. III.

The lasers that generated the coupling and probe fields were injection-locked to a master laser. Because of the injection lock, the contribution of the laser frequency fluctuations to the decoherence rate in the Λ -type EIT system is negligible [2]. In the forward direction, we maintained the frequencies of Ω_{p+} and Ω_{c+} around the resonance frequencies of their transitions ($\Delta_+ \approx 0$), and kept their frequency difference, i.e., their two-photon frequency, to the two-photon resonance. In the backward direction, we also kept the two-photon frequency of Ω_{p-} and Ω_{c-} to the two-photon resonance, but red-detuned their frequencies by about 1.0Γ with respect to their transition frequencies ($\Delta_- = -1.0\Gamma$). A sufficiently large difference between the one-photon detuning in the forward direction, i.e., Δ_+ , and that in the backward direction, i.e., Δ_- , is necessary for the formation of stationary DSPs in cold media [1].

In the system of the two-photon transition (TPT) that

induced the dipole-dipole interaction (DDI), there are a ground state $|2\rangle$ which is the same state $|2\rangle$ in the Λ -type EIT system, an excited state $|4\rangle$ ($|5P_{3/2}, F=3, m_F=2\rangle$), and a Rydberg state $|5\rangle$ ($|32D_{5/2}, m_J=3/2 \& 5/2\rangle$). The spontaneous decay rate of $|4\rangle$ is equal to Γ , and that of $|5\rangle$ is $2\pi \times 7.9$ kHz or $1.3 \times 10^{-3}\Gamma$. The two laser fields drove the transition from $|2\rangle$ to $|4\rangle$ and that from $|4\rangle$ to $|5\rangle$, and they had the Rabi frequencies Ω_a and Ω_b , respectively. Throughout this work, $\Omega_a = 2.0\Gamma$ and $\Omega_b = 1.6\Gamma$ during the TPT. The determination method of Ω_a and Ω_b will be described in Sec. III.

The frequencies of the TPT fields of Ω_a and Ω_b were stabilized with the Pound-Drever-Hall scheme. The root-mean-square value of the two-photon frequency fluctuation is about 150 kHz. We utilized acousto-optic modulators (AOMs) and electro-optic modulators (EOMs) to tune frequencies and to modulate amplitudes of the laser fields. The rf or microwave frequency sources of the AOMs and EOMs were locked to a rubidium frequency standard (SRS FS725). Details of the stabilization and tuning of the laser field frequencies can be found in Ref. [2]. We fixed the sum of the frequencies, i.e., two-photon frequency, of Ω_a and Ω_b to the two-photon resonance, while detuning their frequencies by 5.0Γ with respect to their transition frequencies ($\Delta_a = -\Delta_b = +5.0\Gamma$).

In the Λ -type EIT system, the e^{-1} full width of the input probe beam was $130 \mu\text{m}$, and those of the forward and backward coupling beams were 3.1 mm. The forward and backward coupling fields completely overlapped and covered the entire atom cloud.

In the TPT system, the field of Ω_a propagated in the forward direction and that of Ω_b in the backward direction. This counter-propagation configuration minimized the Doppler effect in the TPT. The e^{-1} full width of the Ω_a beam was 4.9 mm, and that of the Ω_b beam was $250 \mu\text{m}$. The beams of Ω_a and Ω_b fully covered the region of stationary DSPs in the atom cloud.

The output probe field was coupled to a single-mode optical fiber to minimize the background signals from the other light fields, and detected by a photomultiplier tube (PMT). A digital oscilloscope (Agilent MSO6014A) acquired the signal from the PMT. All the timings of Ω_{c+}^2 , Ω_{c-}^2 , Ω_a^2 , and Ω_b^2 were monitored by fast photo detectors. In the measurement of the phase shift of the output probe pulse, we employed the beat-note interferometer [3]. The

*Electronic address: upfell@gmail.com

†Electronic address: yu@phys.nthu.edu.tw

measurement method of the phase shift was the same as that described in Ref. [4].

In the experiment, the optical depth (OD) of the system was maintained around 36. Using a known value of Ω_{c+} in the Λ -type EIT system, we measured the propagation delay time, τ_d , of the slow-light probe pulse to determine the OD, α , where $\tau_d = \alpha\Gamma/\Omega_{c+}^2$ [2]. The ground-state decoherence rate, γ_Λ , affects the coherence involving the DSP, and its value was about $9 \times 10^{-4}\Gamma$ or $2\pi \times 5.4$ kHz in this work. We measured the output transmission of the probe field, T_{SL} , to determine the value of γ_Λ , where $T_{SL} = \exp(-2\alpha\gamma_\Lambda\Gamma/\Omega_{c+}^2)$ [2]. Examples of data for the determinations of the coupling Rabi frequency, optical density, and decoherence rate in a Λ -type EIT system can be found in Fig. 3 of Ref. [2].

II. THEORETICAL MODEL

To make theoretical predictions, we numerically solved the optical Bloch equations (OBEs) of the density-matrix elements of the atoms, $\rho_{ij}(t, z)$, and Maxwell-Schrödinger equations (MSEs) of the forward/backward probe pulses

(with the Rabi frequencies of $\Omega_{p+}(t, z)$ and $\Omega_{p-}(t, z)$), where t and z represent the temporal and spatial variables. There are five energy levels in the calculation consisting of two ground states $|1\rangle$ and $|2\rangle$, two excited states $|3\rangle$ and $|4\rangle$, and a Rydberg state $|5\rangle$. The system of the Λ -type electromagnetically induced transparency (EIT) is formed by $|1\rangle$, $|2\rangle$ and $|3\rangle$. It is driven by the two probe pulses and the forward/backward coupling fields ($\Omega_{c+}(t)$ and $\Omega_{c-}(t)$) to generate the stationary dark-state polariton (DSP) [1]. The coherences of ρ_{31+} and ρ_{31-} correspond to the forward/backward probe transitions, and those of ρ_{32+} and ρ_{32-} to the forward/backward coupling transitions. In the system of the two-photon transition (TPT), the two fields of $\Omega_a(t)$ and $\Omega_b(t)$ drove the transition of $|2\rangle \rightarrow |4\rangle \rightarrow |5\rangle$ with a large one-photon detuning. The coherences of ρ_{42} and ρ_{52} correspond to the transitions of Ω_a and Ω_b , respectively. The TPT excites and deexcites the population between $|2\rangle$ and $|5\rangle$ or, equivalently, converts the coherence of ρ_{21} to that of ρ_{51} and vice versa.

The OBEs describe how the optical fields influence the density-matrix operator, and they are given by

$$\frac{\partial \rho_{21}}{\partial t} = \frac{i}{2}(\Omega_{c+}^* \rho_{31+} + \Omega_{c-}^* \rho_{31-} - \Omega_{p+} \rho_{32+}^* - \Omega_{p-} \rho_{32-}^* + \Omega_a^* \rho_{41}) + i\delta_\Lambda \rho_{21} - \gamma_\Lambda \rho_{21}, \quad (S1)$$

$$\frac{\partial \rho_{31\pm}}{\partial t} = \frac{i}{2}[\Omega_{p\pm}(\rho_{11} - \rho_{33}) + \Omega_{c\pm} \rho_{21}] + i\Delta_{p\pm} \rho_{31\pm} - \frac{\Gamma_3}{2} \rho_{31\pm}, \quad (S2)$$

$$\frac{\partial \rho_{41}}{\partial t} = \frac{i}{2}(\Omega_a \rho_{21} + \Omega_b^* \rho_{51} - \Omega_{p+} \rho_{43+} - \Omega_{p-} \rho_{43-}) + i(\Delta_a + \delta_\Lambda) \rho_{41} - \frac{\Gamma_4}{2} \rho_{41}, \quad (S3)$$

$$\frac{\partial \rho_{51}}{\partial t} = \frac{i}{2}(\Omega_b \rho_{41} - \Omega_{p+} \rho_{53+} - \Omega_{p-} \rho_{53-}) + i(\delta_R + \Delta_{DDI} + \delta_\Lambda) \rho_{51} - \left(\frac{\Gamma_5}{2} + \gamma_R + \gamma_{DDI} + \gamma_\Lambda\right) \rho_{51}, \quad (S4)$$

$$\frac{\partial \rho_{32\pm}}{\partial t} = \frac{i}{2}[\Omega_{c\pm}(\rho_{22} - \rho_{33}) + \Omega_{p\pm} \rho_{21}^* - \Omega_a \rho_{43\pm}^*] + i\Delta_{c\pm} \rho_{32\pm} - \frac{\Gamma_3}{2} \rho_{32\pm}, \quad (S5)$$

$$\frac{\partial \rho_{42}}{\partial t} = \frac{i}{2}[\Omega_a(\rho_{22} - \rho_{44}) + \Omega_b^* \rho_{52} - \Omega_{c+} \rho_{43+} - \Omega_{c-} \rho_{43-}] + i\Delta_a \rho_{42} - \frac{\Gamma_4}{2} \rho_{42}, \quad (S6)$$

$$\frac{\partial \rho_{52}}{\partial t} = \frac{i}{2}(\Omega_b \rho_{42} - \Omega_a \rho_{54} - \Omega_{c+} \rho_{53+} - \Omega_{c-} \rho_{53-}) + i(\delta_R + \Delta_{DDI}) \rho_{52} - \left(\frac{\Gamma_5}{2} + \gamma_R + \gamma_{DDI}\right) \rho_{52}, \quad (S7)$$

$$\frac{\partial \rho_{43\pm}}{\partial t} = \frac{i}{2}(\Omega_a \rho_{32\pm}^* + \Omega_b^* \rho_{53\pm} - \Omega_{p\pm}^* \rho_{41} - \Omega_{c\pm}^* \rho_{42}) + i(\Delta_a - \Delta_{c\pm}) \rho_{43\pm} - \frac{\Gamma_3 + \Gamma_4}{2} \rho_{43\pm}, \quad (S8)$$

$$\frac{\partial \rho_{53\pm}}{\partial t} = \frac{i}{2}(\Omega_b \rho_{43\pm} - \Omega_{c\pm}^* \rho_{52} - \Omega_{p\pm}^* \rho_{51}) + i(\delta_R + \Delta_{DDI} - \Delta_{c\pm}) \rho_{53\pm} - \frac{\Gamma_3 + \Gamma_5}{2} \rho_{53\pm}, \quad (S9)$$

$$\frac{\partial \rho_{54}}{\partial t} = \frac{i}{2}[\Omega_b(\rho_{44} - \rho_{55}) - \Omega_a^* \rho_{52}] + i(\Delta_{DDI} + \Delta_b) \rho_{54} - \frac{\Gamma_4 + \Gamma_5}{2} \rho_{54}, \quad (S10)$$

$$\frac{\partial \rho_{11}}{\partial t} = \frac{i}{2}(\Omega_{p+}^* \rho_{31+} - \Omega_{p+} \rho_{31+}^* + \Omega_{p-}^* \rho_{31-} - \Omega_{p-} \rho_{31-}^*) + \frac{\Gamma_3}{2} \rho_{33}, \quad (S11)$$

$$\frac{\partial \rho_{22}}{\partial t} = \frac{i}{2}(\Omega_{c+}^* \rho_{32+} - \Omega_{c+} \rho_{32+}^* + \Omega_{c-}^* \rho_{32-} - \Omega_{c-} \rho_{32-}^* + \Omega_a^* \rho_{42} - \Omega_a \rho_{42}^*) + \frac{\Gamma}{2} \rho_{33} + \Gamma_4 \rho_{44}, \quad (S12)$$

$$\frac{\partial \rho_{44}}{\partial t} = \frac{i}{2}(\Omega_a \rho_{42}^* - \Omega_a^* \rho_{42} + \Omega_b^* \rho_{54} - \Omega_b \rho_{54}^*) - \Gamma_4 \rho_{44}, \quad (S13)$$

$$\frac{\partial \rho_{55}}{\partial t} = \frac{i}{2}(\Omega_b \rho_{54}^* - \Omega_b^* \rho_{54}) - \Gamma_5 \rho_{55}, \quad (S14)$$

where $\Delta_{c\pm}$ and $\Delta_{p\pm}$ are the one-photon detunings of $\Omega_{c\pm}$ and $\Omega_{p\pm}$, respectively, δ_Λ ($= \Delta_{p+} - \Delta_{c+} = \Delta_{p-} - \Delta_{c-}$) is the two-photon detuning of the Λ -type EIT transitions, γ_Λ is the ground-state decoherence rate, Δ_a and Δ_b are the one-photon detunings of Ω_a and Ω_b , respectively, δ_R ($= \Delta_a + \Delta_b$) is the two-photon detuning of the TPT, γ_R is the Rydberg-state decoherence rate, Δ_{DDI} and γ_{DDI} are the DDI-induced frequency shift and decoherence rate, and Γ_3 ($= \Gamma$ or $2\pi \times 6$ MHz), Γ_4 ($= \Gamma$), and Γ_5 ($= 1.3 \times 10^{-3} \Gamma$) represent the spontaneous decay rates of $|3\rangle$, $|4\rangle$, and $|5\rangle$, respectively.

Since γ_Λ , γ_R , $\gamma_{\text{DDI}} \ll \Gamma$ in the experiment, these three decoherence rates do not appear in the time-derivative equations of $\rho_{53\pm}$ and ρ_{54} in the calculation. Furthermore, $\Gamma_5 \ll \Gamma$, $\Gamma_5 \ll \gamma_R$, and $\Gamma_5^{-1} \gg$ the TPT duration in the experiment. Thus, we set $\Gamma_5 = 0$ in the calculation, which did not change the outcome. The forward probe and coupling fields had $\Delta_{c+} = \Delta_{p+} \equiv \Delta_+ \approx 0$, and the backward probe and coupling fields had $\Delta_{c-} = \Delta_{p-} \equiv \Delta_- = -1.0\Gamma$. Such an arrangement of the one-photon detunings suppressed possible high-order coherences, which could be established by the counter-propagating fields of Ω_{p+} and Ω_{c-} (Ω_{p-} and Ω_{c+}) [1]. Consequently, we do not need to consider the high-order coherences in the calculation.

In the present work, the experimental condition satisfied the weak-interaction regime, i.e., $(r_B/r_a)^3 \ll 1$ where r_B is the blockade radius and r_a is the half mean distance between Rydberg atoms. Hence, Δ_{DDI} and γ_{DDI} in the OBEs are given by [4–6]

$$\Delta_{\text{DDI}} = A\rho_{55}, \quad (\text{S15})$$

$$\gamma_{\text{DDI}} = A\rho_{55}, \quad (\text{S16})$$

where A represents the frequency shift (also the decoherence rate) per unit population of $|5\rangle$, and its value depends on the atomic density in the system and the DDI strength. The appearances of Δ_{DDI} and γ_{DDI} make the OBEs nonlinear. The OBEs involving the DDI effect are very similar to those in our previous works of Refs. [4, 5], which were derived based on the mean field model studied in Ref. [6]. In those works, the theoretical predictions are in agreement with the experimental data.

The MSEs describe how the forward and backward probe fields are affected by the atomic coherences, and they are given by

$$\frac{1}{c} \frac{\partial}{\partial t} \Omega_{p+} + \frac{\partial}{\partial z} \Omega_{p+} = i \frac{\alpha \Gamma}{2L} \rho_{31+}, \quad (\text{S17})$$

$$\frac{1}{c} \frac{\partial}{\partial t} \Omega_{p-} - \frac{\partial}{\partial z} \Omega_{p-} + i \Delta_k \Omega_{p-} = i \frac{\alpha \Gamma}{2L} \rho_{31-}, \quad (\text{S18})$$

where α and L are the optical depth and length of the atom cloud, and $\Delta_k \equiv (\vec{k}_{p-} - \vec{k}_{c-} - \vec{k}_{p+} + \vec{k}_{c+}) \cdot \hat{z}$ and $\vec{k}_{p\pm}$ and $\vec{k}_{c\pm}$ are the wave vectors of $\Omega_{p\pm}$ and $\Omega_{c\pm}$, respectively. The value of $L\Delta_k$ is the degree of phase mismatch in the system. Although Δ_k only appears in the MSE of Ω_{p-} , it reduces the energies of Ω_{p+} and Ω_{p-} equally due to the coupling between the forward and backward fields, i.e., the four-wave mixing process [7–9].

III. DETERMINATION OF THE RABI FREQUENCIES

In this section, we illustrate the methods that determine the Rabi frequencies of the forward and backward coupling fields Ω_{c+} and Ω_{c-} , and that of the two-photon-transition (TPT) field Ω_a . We also checked whether the Rabi frequency of the TPT field Ω_b determined by the data in Fig. 2(b) of the main text is reasonable.

The Autler-Townes splitting (ATS) in the EIT transmission spectrum was used to determine the Rabi frequencies of Ω_{c+} and Ω_{c-} . Figure S1 shows the representative EIT spectra. We followed the determination method described in Ref. [2]. The frequency difference between two transmission minima, δ_+ and δ_- , gave the Rabi frequency. As mentioned in the reference, the optical depth (OD) of the atom cloud was reduced to a value between 1 and 2 in the measurement of the spectrum. At a low OD, the minima can be clearly identified, and any asymmetry in the spectrum due to a nonzero one-photon detuning of the coupling field can be noticed. In the EIT system,

$$\delta_+ - \delta_- \approx \Omega + \Delta^2/2\Omega, \quad (\text{S19})$$

where Ω is the coupling Rabi frequency and Δ is the one-photon detuning. As long as $\Delta^2 \ll \Omega^2$, the angular-frequency separation between δ_+ and δ_- is nearly the same as Ω .

In the Λ -type EIT system, we employed the forward probe field (Ω_{p+}) to measure the values of the forward and backward coupling Rabi frequencies, Ω_{c+} and Ω_{c-} , as shown in Figs. S1(a) and S1(b), respectively. The sweeping of the probe frequency deviated the probe propagation direction very little. Since the propagation direction of Ω_{c-} was opposite to that of Ω_{p+} , the Doppler effect made the decoherence rate in Fig. S1(b) much larger than that in Fig. S1(a). Consequently, the EIT peak transmission in Fig. S1(b) is significantly reduced, and that in Fig. S1(a) is nearly 100%. Nevertheless, the frequency separation between the two transmission minima is not affected by the decoherence rate.

To determine the value of Ω_a of the TPT field, we utilized the all-optical switching (AOS) effect in the four-level N -type system [10, 11], which consists of states $|1\rangle$, $|2\rangle$, $|3\rangle$, and $|4\rangle$ in this work. In the AOS, the forward probe (Ω_{p+}) and coupling (Ω_{c+}) fields form the Λ -type EIT configuration, and the presence of the field of Ω_a causes an additional attenuation of the output probe field. As shown in the inset of Fig. S2, we first stored the probe pulse in the atoms, then applied the pulse of Ω_a during the storage time, and finally retrieved the probe pulse. The one-photon detuning, Δ_a , of the Ω_a pulse was kept to $+5.0\Gamma$ in the measurement. Except that the fields of Ω_{c-} and Ω_b were absent, all the other experimental arrangements were the same as those in the measurement with the TPT. In Fig. S2, the circles and black line are the experimental data and best fit of the retrieved probe energy transmission, T_{AOS} , as a function of the Ω_a pulse

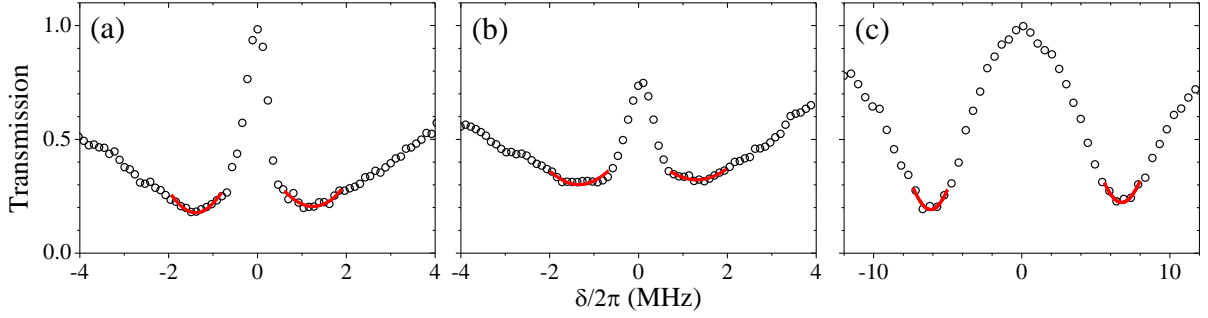


FIG. S1: (a) [or (b)] Probe transmission spectrum as a function of the two-photon detuning, δ , under the constant presence of the forward (or backward) coupling field of Ω_{c+} (or Ω_{c-}) in the Λ -type EIT system, and (c) that under the constant presence of the TPT field of Ω_b in the Rydberg-EIT system. In the measurement of each spectrum, the one-photon detuning was nearly zero. Black circles are the experimental data. Red curves are the best fits to determine the frequencies of minima. The frequency separation between the two minima gives the Autler-Townes splitting of (a) 0.44Γ , (b) 0.44Γ , or (c) 2.0Γ .

duration, τ_a . The fitting function is given by

$$T_{\text{AOS}} = T_0 \exp\left(-\frac{\Omega_a^2 \Gamma}{\Gamma^2 + 4\Delta_a^2} \tau_a\right), \quad (\text{S20})$$

where T_0 is the transmission without the presence of Ω_a . The best fit determined the value of Ω_a used in the TPT.

We measured the ATS induced by the TPT field Ω_b in a Rydberg-EIT system [2]. In the system, the coupling field Ω_b and a weak probe field drove the transition of $|5P_{3/2}, F=3, m_F=3\rangle \rightarrow |32D_{5/2}, m_J=5/2\rangle$ and that of $|5S_{1/2}, F=2, m_F=2\rangle \rightarrow |5P_{3/2}, F=3, m_F=3\rangle$, respectively, and the two fields counter-propagated. The input probe Rabi frequency was set to about 0.05Γ such that the DDI effect was negligible. Figure S1(c) shows

the Rydberg-EIT spectrum taken at a nearly zero one-photon detuning. The ATS in the spectrum is 2.0Γ . However, the transition of Ω_b in Fig. S1(c) was not the same as that of Ω_b in the TPT, which was from $|5P_{3/2}, F=3, m_F=2\rangle$ to $|32D_{5/2}, m_J=3/2 \text{ \& } 5/2\rangle$. According to the ATS and the Clebsch-Gordan coefficients, the Rabi frequency of the transition to $|32D_{5/2}, m_J=5/2\rangle$ and that to $|32D_{5/2}, m_J=3/2\rangle$ should be 1.4Γ and 1.1Γ , respectively. Their root-mean-square value is 1.8Γ . It is reasonable that the TPT field Ω_b had the Rabi frequency of 1.6Γ as determined by Fig. 2(b) of the main text.

IV. DEGREE OF PHASE MISMATCH DURING THE STATIONARY DARK-STATE POLARITON

The stationary dark-state polariton (DSP) was formed by the balance between the two four-wave mixing (FWM) processes of $\Omega_{p+} - \Omega_{c+} + \Omega_{c-} \rightarrow \Omega_{p-}$ and $\Omega_{p-} - \Omega_{c-} + \Omega_{c+} \rightarrow \Omega_{p+}$ [8], where $\Omega_{p\pm}$ and $\Omega_{c\pm}$ denote the forward/backward probe and coupling fields, respectively. The former process consists of absorbing a forward probe photon, emitting a forward coupling photon, and absorbing a backward coupling photon to finally generate a backward probe photon. The latter process is just the reversed former process to generate a forward probe photon from a backward probe photon. In the FWM, the phase mismatch causes an additional attenuation of the stationary DSP, and its measure, i.e., the degree of the phase mismatch, is given by $L\Delta_k$, where L is the medium length and Δ_k represents the sum of the wave vectors of the four fields projected on the propagation direction. Please see Eqs. (S17) and (S18) for the role of $L\Delta_k$ in the Maxwell-Schrödinger equations. The definition and details of Δ_k are given right after the equations.

To determine the value of $L\Delta_k$ in the stationary-DSP experiment, we measured the retrieved probe energy as a function of the stationary-DSP duration. The experimental condition or parameters of the measurement was the same as that of Fig. 2(a) of the main text. As shown

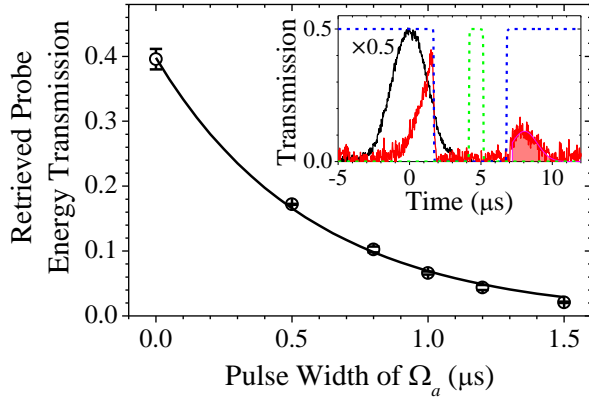


FIG. S2: Main plot: In the system of all-optical switching (AOS), transmission of the retrieved probe energy versus the pulse duration of the field of Ω_a . Circles are the experimental data taken at $\Delta_a = 5.0\Gamma$. Black line is the best fit with the fitting function given by Eq. (S20), which determines $\Omega_a = 2.0\Gamma$. Inset: Black and red lines are the signals of the probe pulses without and with the atoms, respectively. The black line is scaled down by a factor of 0.5. Blue and green dashed lines represent the time sequences of the coupling field and the field of Ω_a . Filled area in red represents the retrieved probe energy after the AOS effect.

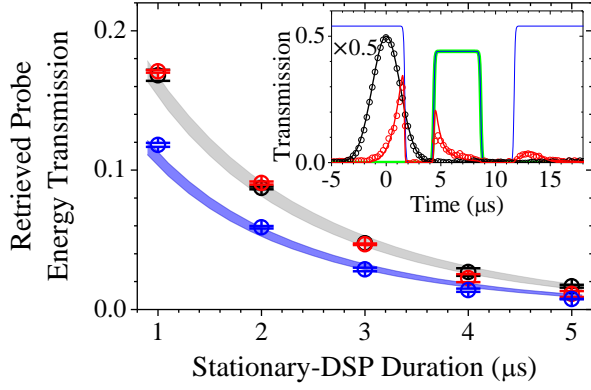


FIG. S3: Main plot: Transmission of the retrieved probe energy versus the stationary-DSP duration. Black, red, and blue circles are the experimental data taken at $\Omega_{p0} = 0.07\Gamma$, 0.24Γ , and 0.40Γ , respectively, where Ω_{p0} is the peak Rabi frequency of the input probe pulse. Gray ($\Omega_{p0} = 0.07\Gamma$ and 0.24Γ) and blue ($\Omega_{p0} = 0.40\Gamma$) areas are the theoretical predictions calculated with $L\Delta_k = 0.90$ rad. The experimental parameters were $\alpha = 36 \pm 1$, $\Omega_{c+} = 0.54\Gamma$ before the storage and after the retrieval, $\Omega_{c+} = \Omega_{c-} = 0.44\Gamma$ during the stationary DSP, and $\gamma_\Lambda = (9 \pm 1) \times 10^{-4}\Gamma$. Thicknesses of the gray and blue areas represent the uncertainties or fluctuations in the OD and ground-state decoherence rate. Inset: Representative data of the probe signals without (black circles) and with (red circles) the atom cloud. Black (red) line is the best fit (theoretical prediction) of the black (red) circles. The black circles and line are scaled down by a factor of 0.5. Blue and green lines represent the timing sequence of Ω_{c+} and Ω_{c-} , the two lines completely overlap during the stationary DSP ($4 \mu s < t < 9 \mu s$ here). The red circles underneath the green-line pulse reveal that during the stationary DSP the probe light leaked out of the atoms in the forward direction.

in the inset of Fig. S3, we first stored the probe pulse in the atoms, then applied the pulse of the forward and backward coupling fields to generate the stationary DSP for a given duration, τ_{DSP} , and finally retrieved the probe pulse after the execution of τ_{DSP} . The time length from storing to retrieving the probe pulse was fixed to about $10 \mu s$ to accommodate the variation of the stationary-DSP duration. The main plot of Fig. S3 shows the retrieved probe energy transmission versus τ_{DSP} at three different values of the peak Rabi frequency, Ω_{p0} , of the input probe pulse. In the figure, the circles are the experimental data. The retrieved probe energy transmissions of $\Omega_{p0} = 0.07\Gamma$ and 0.24Γ are about the same, but is higher than that of $\Omega_{p0} = 0.40\Gamma$. As $\Omega_{p0} \leq 0.24\Gamma$, the probe pulse is weak enough to be treated as the perturbation, and the result does not depend on Ω_{p0} . On the other hand, as Ω_{p0} becomes larger, the probe pulse is no longer the perturbation and its intensity influences the outcome.

In Fig. S3, the colored areas represent the theoretical predictions. We used the experimentally-determined values of the optical density (α), the forward and backward coupling Rabi frequencies (Ω_{c+} and Ω_{c-}), and the ground-state decoherence rate (γ_Λ) in the theoretical cal-

culation. The determination methods of α and γ_Λ can be found in the last paragraph of Sec. I, and that of Ω_{c+} and Ω_{c-} in the second and third paragraphs of Sec. III. Due to the fluctuations in α and γ_Λ , the prediction of each Ω_{p0} is displayed as an area. A single value of $L\Delta_k$ of 0.9 rad was used in all the predictions such that the consistency between the data and predictions is satisfactory as shown in Fig. S3. This nonzero $L\Delta_k$ can be caused by a little misalignment among the fields in the FWM processes.

V. ESTIMATION OF THE COEFFICIENT A OF DIPOLE-DIPOLE INTERACTION

We estimate the strength of dipole-dipole interaction (DDI) or the coefficient A with a simplified model in this section, where A is defined as the DDI-induced decoherence rate, γ_{DDI} , and frequency shift, Δ_{DDI} , per unit Rydberg-state population, ρ_{55} , as shown by Eqs. (S15) and (S16). The coefficient A was used in the equations of the coherences ρ_{51} , ρ_{52} , ρ_{53} , and ρ_{54} relating to the Rydberg state $|5\rangle$, i.e., Eqs. (S4), (S7), (S9), and (S10), respectively. In the experiment, we utilized a series of measurements of the output probe energy transmission against the input probe intensities or Ω_{p0}^2 to determine $A = 0.60\Gamma$ as shown by Fig. 2 of the main text.

The formation of stationary dark-state polaritons (DSP) is not relevant to the DDI strength. Consequently, state $|3\rangle$ and the probe and coupling fields are not present in the model here. To focus on the DDI effect, we only consider states $|1\rangle$, $|2\rangle$, and $|5\rangle$. An effective field with the Rabi frequency of Ω_{eff} drives the one-photon transition (OPT) between $|2\rangle$ and $|5\rangle$. Due to a large one-photon detuning, Δ_a , in the experiment, the intermediate state $|4\rangle$ of the two-photon transition (TPT) can be eliminated. Thus, the TPT of $|2\rangle \leftrightarrow |4\rangle \leftrightarrow |5\rangle$ with the driving fields of Ω_a and Ω_b in the experiment is equivalent to the OPT of $|2\rangle \leftrightarrow |5\rangle$ here, and

$$\Omega_{\text{eff}} \approx \frac{\Omega_a \Omega_b}{2\Delta_a}. \quad (\text{S21})$$

Considering $\Omega_a = 2.0\Gamma$, $\Omega_b = 1.6\Gamma$, and $\Delta_a = 5.0\Gamma$ of the TPT in the experiment, $\Omega_{\text{eff}} = 0.32\Gamma$ in the OPT.

The OPT drives the Rabi oscillation between $|2\rangle$ and $|5\rangle$, and the equations of motion are given by

$$\frac{\partial \rho_{55}}{\partial t} = \frac{i}{2}(\Omega_{\text{eff}} \rho_{52}^* - \Omega_{\text{eff}}^* \rho_{52}), \quad (\text{S22})$$

$$\frac{\partial \rho_{52}}{\partial t} = \frac{i}{2}\Omega_{\text{eff}}(\rho_{22} - \rho_{55}) + iA\rho_{55}\rho_{52} - A\rho_{55}\rho_{52}, \quad (\text{S23})$$

$$\rho_0 = \rho_{22} + \rho_{55}, \quad (\text{S24})$$

where $A\rho_{55}$ is substituted for γ_{DDI} and Δ_{DDI} and ρ_0 is the initial total population in the system. In the above equations, we neglect the spontaneous decay rate of $|5\rangle$ (i.e., Γ_5) and all the other decoherence rates (i.e., γ_Λ and γ_R), which appear in Eqs. (S1)-(S14).

The OPT also converts the coherences ρ_{21} and ρ_{51} back and forth, and the equations of the conversion are given by

$$\frac{\partial \rho_{21}}{\partial t} = \frac{i}{2} \Omega_{\text{eff}} \rho_{51}, \quad (\text{S25})$$

$$\frac{\partial \rho_{51}}{\partial t} = \frac{i}{2} \Omega_{\text{eff}} \rho_{21} + i\omega \rho_{51} - \gamma \rho_{51}, \quad (\text{S26})$$

where ω and γ correspond to the detuning and decoherence rate of the OPT. Since the output probe energy transmission is proportional to $|\rho_{21}|^2$, we are interested in the solution of ρ_{21} given by

$$\text{Re}[\rho_{21}(\omega, \gamma)] \approx \sqrt{\rho_0} e^{-\gamma t/2} \left[\cos\left(\frac{\omega t}{2}\right) \cos\left(\frac{\Omega' t}{2}\right) + \frac{\omega}{\Omega'} \sin\left(\frac{\omega t}{2}\right) \sin\left(\frac{\Omega' t}{2}\right) + \frac{\gamma}{\Omega'} \cos\left(\frac{\omega t}{2}\right) \sin\left(\frac{\Omega' t}{2}\right) \right], \quad (\text{S27})$$

$$\text{Im}[\rho_{21}(\omega, \gamma)] \approx \sqrt{\rho_0} e^{-\gamma t/2} \left[\sin\left(\frac{\omega t}{2}\right) \cos\left(\frac{\Omega' t}{2}\right) - \frac{\omega}{\Omega'} \cos\left(\frac{\omega t}{2}\right) \sin\left(\frac{\Omega' t}{2}\right) + \frac{\gamma}{\Omega'} \sin\left(\frac{\omega t}{2}\right) \sin\left(\frac{\Omega' t}{2}\right) \right], \quad (\text{S28})$$

$$|\rho_{21}(\omega, \gamma)|^2 \approx \rho_0 e^{-\gamma t} \left\{ \frac{1}{2} [1 + \cos(\Omega' t)] + \frac{\gamma}{\Omega'} \sin(\Omega' t) + \frac{\gamma^2}{2\Omega'^2} [1 - \cos(\Omega' t)] + \frac{\omega^2}{2\Omega'^2} [1 - \cos(\Omega' t)] \right\}, \quad (\text{S29})$$

$$\Omega' \equiv \sqrt{\Omega_{\text{eff}}^2 + \omega^2}. \quad (\text{S30})$$

To estimate the value of A , we utilized the mean-field approach based on the probability function of nearest-neighbor distribution (NND) [6, 12]. Considering Rydberg atoms are randomly distributed, the probability of finding the DDI-induced frequency shift within ω and $\omega + d\omega$ is given by

$$P(\omega) = \frac{1}{\omega_a} \frac{\left[1 + \sqrt{1 + 4(\omega/\omega_a)}\right]^2}{4(\omega/\omega_a)^2 \sqrt{1 + 4(\omega/\omega_a)}} \times \exp\left[-\frac{1 + \sqrt{1 + 4(\omega/\omega_a)}}{2(\omega/\omega_a)}\right], \quad (\text{S31})$$

where

$$\omega_a \equiv |C_6|/r_a^6, \quad (\text{S32})$$

C_6 is the van der Waals coefficient, r_a is the half-mean distance between the Rydberg atoms given by

$$(4\pi/3)r_a^3 \equiv (n_{\text{atom}}\rho_{55})^{-1}, \quad (\text{S33})$$

and n_{atom} is the atomic density. The derivation of $P(\omega)$ using the NND can be found in Ref. [6]. We performed the following integrals to simulate the DDI effect:

$$\bar{\rho}_{21,r}(t) = \int_0^\infty d\omega P(\omega) \text{Re}[\rho_{21}(\omega, \gamma = 0)], \quad (\text{S34})$$

$$\bar{\rho}_{21,i}(t) = \int_0^\infty d\omega P(\omega) \text{Im}[\rho_{21}(\omega, \gamma = 0)], \quad (\text{S35})$$

$$|\bar{\rho}_{21}|^2 \equiv [\bar{\rho}_{21,r}(t)]^2 + [\bar{\rho}_{21,i}(t)]^2. \quad (\text{S36})$$

Because of the distribution function $P(\omega)$, $|\bar{\rho}_{21}|^2$ is a function of ρ_{55} as indicated by Eqs. (S31)-(S33).

The process of the estimation of A is illustrated as the followings: (i) We set $A = 0$ and numerically solved

Eqs. (S22)-(S24) to obtain $\rho_{55}(t)$ as shown by the black circles in Fig. S4(a). (ii) With $\rho_{55}(t)$, we used Eqs. (S34)-(S36) to evaluate the temporal data points of $|\bar{\rho}_{21}|^2$ represented by the black circles in Fig. S4(b). (iii) The data points in Fig. S4(b) are fitted with the function of

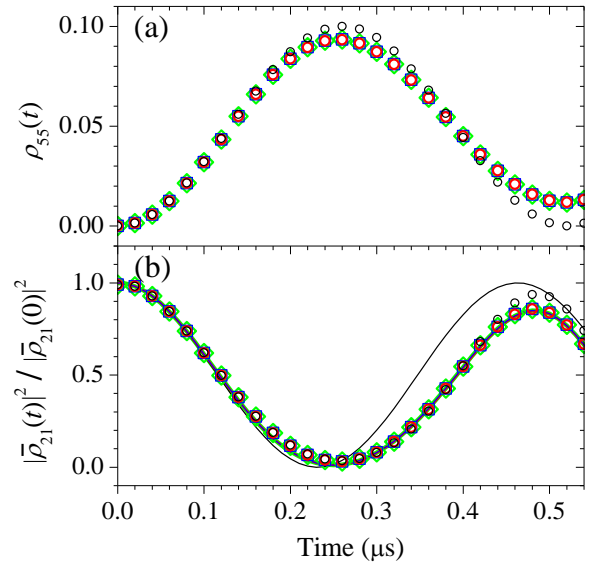


FIG. S4: Estimation of the DDI strength or coefficient A . (a) The solution of $\rho_{55}(t)$ by numerically solving Eqs. (S22)-(S24). (b) The ensemble average of the microscopic DDI effect, i.e., $|\bar{\rho}_{21}|^2$ calculated from Eqs. (S34)-(S36). Black circles, red circles, blue squares, and green diamonds represent the results from the first to the fourth iterations. Lines represent the corresponding best fits with the fitting function of $|\rho_{21}(\omega = A\rho_{55}, \gamma = A\rho_{55})|^2$ given by Eq. (S29), in which A is the fitting parameter.

$|\rho_{21}(\omega = A\rho_{55}, \gamma = A\rho_{55})|^2$ shown by Eq. (S29), where A is the only fitting parameter. The fitting means to relate the ensemble average of the microscopic DDI effect to the macroscopic quantity A , i.e.,

$$|\bar{\rho}_{21}|^2 = |\rho_{21}(\omega = A\rho_{55}, \gamma = A\rho_{55})|^2. \quad (\text{S37})$$

The black line in Fig. S4(b) is the best fit, which determined the value of A in the first iteration, denoted as $A^{(1)}$. (iv) In the second iteration, we started with the value of $A^{(1)}$ in Eqs. (S22)-(S24) and solved the equations to obtain $\rho_{55}^{(2)}(t)$ as shown by the red circles in Fig. S4(a). Steps (ii) and (iii) were repeated, and the red circles and line in Fig. S4(b) are the results, giving $A^{(2)}$. (v) The process of (i) \rightarrow (ii) \rightarrow (iii) was performed several times until the results converged as demonstrated by the blue squares/line and green diamonds/line in Figs. S4(a) and S4(b).

In the estimation, we set $C_6 = -2\pi \times 130 \text{ MHz} \cdot \mu\text{m}^6$, $n_{\text{atom}} = 0.05 \mu\text{m}^{-3}$, and $\Omega_{\text{eff}} = 0.32\Gamma$ according to the experimental condition. Considering the population of $|2\rangle$ achievable in this work, the value of A estimated by the method in this section depends on ρ_0 very little. As the estimation gives A of 0.54Γ , the experimentally determined A of 0.60Γ sounds reasonable.

VI. THE INPUT PROBE PULSE WITH A LARGE RABI FREQUENCY

We employed the input probe pulses with five different peak Rabi frequencies, Ω_{p0} , of 0.07Γ , 0.2Γ , 0.24Γ , 0.3Γ , 0.4Γ in the experiment. As $\Omega_{p0} \leq 0.24\Gamma$, the experimental data of slow light were well consistent with the theoretical predictions. As $\Omega_{p0} \geq 0.3\Gamma$, the experimental data of slow light deviated from the theoretical predictions. A representative example of the discrepancy taken at Ω_{p0} of 0.4Γ is shown in Fig. S5(a). In the theoretical calculations, we used the parameters of the coupling Rabi frequency (Ω_{c+}), optical depth or OD (α), and ground-state decoherence rate (γ_A), which were determined experimentally by the methods described in Sec. III and in the last paragraph of Sec. I. The determinations were carried out at the experimental condition that the typical electromagnetically induced transparency (EIT) criterion, i.e., $\Omega_{p0}^2 \ll \Omega_{c+}^2$ and $2\gamma\Gamma \ll \Omega_{c+}^2$, is satisfied.

The comparison between the experimental data and theoretical predictions in Fig. S5(a) leads to the following observations: (i) The experimental output pulse peak is smaller than the theoretical one, (ii) the experimental output pulse width is broader than the theoretical one, and (iii) the experimental propagation delay time is approximately the same as the theoretical one. These observations can explain the results of the output probe energies without and with the two-photon transition (TPT).

Figure S5(b) shows the input and output probe pulses without the presence of the TPT. The timing sequences of the forward (Ω_{c+}) and backward (Ω_{c-}) coupling fields are nearly the same as those shown in Fig. 2(a) of the

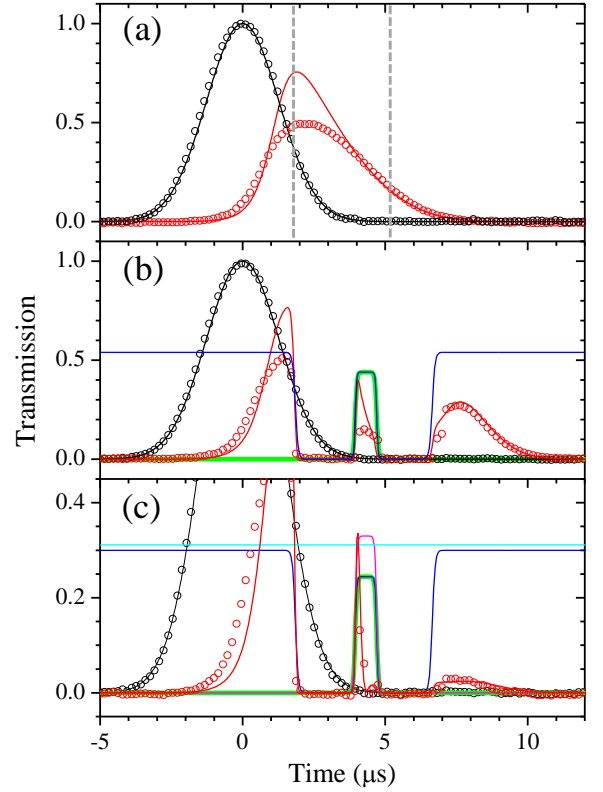


FIG. S5: (a) Slow light under the constant presence of the coupling field. (b, c) The formation of the stationary DSP without and with the TPT or equivalently DDI, respectively. $\Omega_{p0} = 0.4\Gamma$, and all the other experimental parameters are the same as those shown in the caption of Fig. 2 of the main text. Black and red circles are the experimental data of the input and output probe pulses. Black lines represent the Gaussian best fits and red lines are the theoretical predictions. Blue, green, magenta, and cyan lines show the timing sequences of the coupling fields of Ω_{c+} and Ω_{c-} as well as the TPT fields of Ω_a and Ω_b . The part of the probe pulse between the two vertical gray dashed lines in (a) was stored in the atoms at $t \approx 6.0 \mu\text{s}$ (when Ω_{c+} was switched off) in (b) and (c).

main text. As we switched off Ω_{c+} at $t \approx 2.0 \mu\text{s}$, the stored probe energy of the experimental data was less than that of the theoretical prediction due to the observation (i). This first factor could make the experimental probe energy less than the predicted one at the output stage, i.e., $t \gtrsim 6.6 \mu\text{s}$. Nevertheless, the stored probe pulse shape of the experimental data had a smoother spatial variation than that of the theoretical prediction due to the observation (ii). A smoother pulse shape indicates a narrower frequency bandwidth, which makes the energy loss less during the formation of stationary dark-state polaritons (DSPs) [1, 13], i.e., the duration of the green plus and blue pulse in Fig. S5(b). A narrower frequency bandwidth also makes the energy loss less during the pulse propagation at the output stage [14]. This second factor could make the experimental output probe energy more than the predicted. Finally, the medium of EIT plus sta-

tionary DSP can be viewed as a frequency plus spatial bandpass filter. This third factor can make the output probe pulse shape is approximately independent of the input one. Putting the three factors together, we can expect that the experimental and theoretical output probe pulses are consistent as demonstrated by Figs. S5(b) and S5(c), and also by the rightmost blue- and red-circle data points and their corresponding predictions in Fig. 2(c) of the main text.

When the probe Rabi frequency is comparable to the coupling Rabi frequency as well as the spontaneous decay rate in the EIT system, the EIT effect is no longer independent of the probe Rabi frequency. We think a three-dimensional calculation of the optical Bloch equations and the Maxwell-Schrödinger equation is necessary to make a precise theoretical prediction of the slow light. Nevertheless, the three-dimensional calculation is beyond the scope of this work. The discrepancy between the experimental data and theoretical prediction at a large input probe Rabi frequency can be explained, and it does not affect the conclusion of this work at all.

VII. THE DDI-INDUCED PHASE SHIFT UNDER THE RABI OSCILLATION

When we applied the two-photon transition (TPT) in the experiment, it not only produced the Rabi oscillation between the ground state $|2\rangle$ and the Rydberg state $|5\rangle$ but also induced the dipole-dipole interaction (DDI). The Rabi oscillation alone resulted in a phase shift of the ground-state coherence ρ_{21} , and the DDI added an extra phase shift to ρ_{21} . Note that the phase shift of ρ_{21} was transferred to that of the output probe pulse after the retrieval [11].

Figure S6(a) shows the theoretical predictions, elucidating the phase shift of ρ_{21} induced by the Rabi oscillation and also that induced by the DDI. To enhance the DDI-induced phase shift, the decay rates γ_A , γ_R , γ_{DDI} , and Γ_4 as well as the degree of phase mismatch $L\Delta_k$ were set to zero in the calculation of the predictions. We varied the value of A to switch off or on the DDI-induced phase shift, i.e., DDI-induced frequency shift or $\Delta_{DDI} = A\rho_{55}$. In Fig. S6(a), the black solid line represents the result of $A = 0$, i.e., the DDI is switched off, and it reveals the oscillation of the phase shift, which is the consequence of the Rabi oscillation. The black dashed is the baseline of the oscillation. At $A = 0.60\Gamma$, the red solid line represents the result of the phase shift produced by the DDI together with the Rabi oscillation. The red dashed is the baseline of the oscillation. Thus, the phase difference between the red and black dashed lines is solely caused by the DDI. As the interaction time gets longer, the DDI-induced phase shift becomes larger as expected.

We next consider a more realistic case by restoring all the decay terms in the calculation. The values of the decay rates γ_A , γ_R , Γ_4 , and $L\Delta_k$ were set to those specified in the caption of Fig. 2 of the main text, and the DDI-

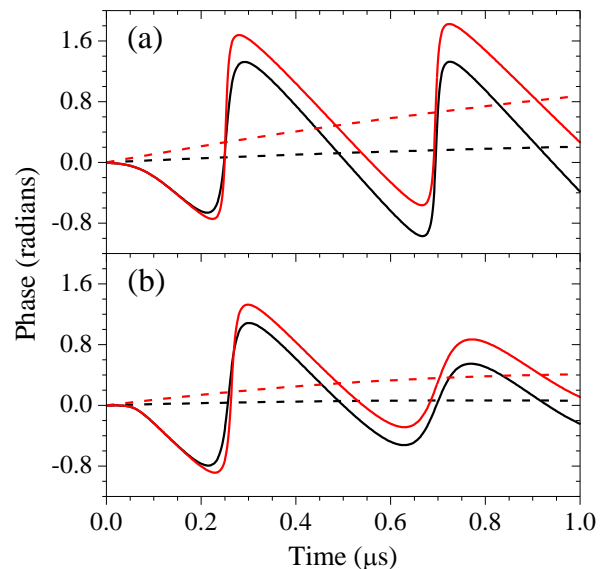


FIG. S6: Simulations of the phase shift of the ground-state coherence ρ_{21} , or equivalently the phase shift of the output probe pulse, as a function of time. Black and red lines are the results without and with the DDI of $A = 0.60\Gamma$, respectively. In the simulations, $\Omega_{p0} = 0.24\Gamma$, $\Delta_- = 0$, $\Omega_a = \Omega_b = 2.0\Gamma$, and the remaining parameters are the same as those in the caption of Fig. 2 of the main text. All decay and decoherence mechanisms are switched off in (a) and intact in (b). Dashed lines represent the baselines of the oscillations. In each subfigure, the difference between the two dashed lines reveals the DDI-induced phase shift.

induced attenuation was brought back, i.e., $\gamma_{DDI} = A\rho_{55}$. In Fig. S6(b), the black and red solid lines are the results without and with the DDI of $A = 0.60\Gamma$. The difference between the black and red dashed lines corresponds to the DDI-induced phase shift. Due to the decay terms, the amount of the DDI-induced phase shift is reduced.

In the simulations for the results shown in Figs. S6(a) and S6(b), we made the two TPT fields have the same Rabi frequency, i.e., $\Omega_a = \Omega_b = 2.0\Gamma$, and set the backward coupling field frequency to the resonance of its transition, i.e., $\Delta_- = 0$. The remaining calculation parameters are the same as the experimental parameters shown in the caption of Fig. 2 of the main text. In the experiment, $\Omega_a (= 2.0\Gamma) \neq \Omega_b (= 1.6\Gamma)$ and $\Delta_- = -1\Gamma$. Both $\Omega_a \neq \Omega_b$ and $\Delta_- = -1\Gamma$ can induce AC Stark shifts, which produces a phase shift to ρ_{21} . Nevertheless, the phase shifts produced by the causes of the Rabi oscillation, $\Omega_a \neq \Omega_b$, and $\Delta_- = -1\Gamma$ depend on the input probe Rabi frequency a little. In Fig. 3(b) of the main text, the data points are the results that the measured phase shifts at different values of the input probe Rabi frequency, Ω_{p0} , were subtracted by that at the smallest value of Ω_{p0} . Therefore, the phase shifts revealed by these data points are mainly contributed from the DDI.

-
- [1] Y.-W. Lin, W.-T. Liao, T. Peters, H.-C. Chou, J.-S. Wang, H.-W. Cho, P.-C. Kuan, and I. A. Yu, "Stationary Light Pulses in Cold Atomic Media and without Bragg Gratings," *Phys. Rev. Lett.* **102**, 213601 (2009).
 - [2] B. Kim, K.-T. Chen, C.-Y. Hsu, S.-S. Hsiao, Y.-C. Tseng, C.-Y. Lee, S.-L. Liang, Y.-H. Lai, J. Ruseckas, G. Juzeliūnas, and I. A. Yu, "Effect of laser-frequency fluctuation on the decay rate of Rydberg coherence," *Phys. Rev. A* **100**, 013815 (2019).
 - [3] Y.-F. Chen, Y.-C. Liu, Z.-H. Tsai, S.-H. Wang, and I. A. Yu, "Beat-note interferometer for direct phase measurement of photonic information," *Phys. Rev. A* **72**, 033812 (2005).
 - [4] B. Kim, K.-T. Chen, S.-S. Hsiao, S.-Y. Wang, K.-B. Li, J. Ruseckas, G. Juzeliūnas, T. Kirova, M. Auzinsh, Y.-C. Chen, Y.-F. Chen, and I. A. Yu, "A weakly-interacting many-body system of Rydberg polaritons based on electromagnetically induced transparency," *Commun. Phys.* **4**, 101 (2021).
 - [5] K.-T. Chen, B. Kim, C.-C. Su, S.-S. Hsiao, S.-J. Huang, W.-T. Liao, and I. A. Yu, "Increasing the decoherence rate of Rydberg polaritons due to accumulating dark Rydberg atoms," *Phys. Rev. Research* **4**, 023024 (2022).
 - [6] S.-S. Hsiao, K.-T. Chen, and I. A. Yu, "Mean field theory of weakly-interacting Rydberg polaritons in the EIT system based on the nearest-neighbor distribution," *Opt. Express* **28**, 28414 (2020).
 - [7] D. A. Braje, V. Balić, S. Goda, G. Y. Yin, and S. E. Harris, "Frequency Mixing Using Electromagnetically Induced Transparency in Cold Atoms," *Phys. Rev. Lett.* **93**, 183601 (2004).
 - [8] Y.-H. Chen, M.-J. Lee, W. Hung, Y.-C. Chen, Y.-F. Chen, and I. A. Yu, "Demonstration of the Interaction between Two Stopped Light Pulses," *Phys. Rev. Lett.* **108**, 173603 (2012).
 - [9] K.-F. Chang, T.-P. Wang, C.-Y. Chen, Y.-H. Chen, Y.-S. Wang, Y.-F. Chen, Y.-C. Chen, and I. A. Yu, "Low-loss high-fidelity frequency beam splitter with tunable split ratio based on electromagnetically induced transparency," *Phys. Rev. Research* **3**, 013096 (2021).
 - [10] C.-Y. Wang, Y.-F. Chen, S.-C. Lin, W.-H. Lin, P.-C. Kuan, and I. A. Yu, "Low-light-level all-optical switching," *Opt. Lett.* **31**, 2350 (2006).
 - [11] Y.-F. Chen, C.-Y. Wang, S.-H. Wang, and I. A. Yu, "Low-Light-Level Cross-phase-Modulation Based on Stored Light Pulses," *Phys. Rev. Lett.* **96**, 043603 (2006).
 - [12] S. Chandrasekhar, "Stochastic problems in physics and astronomy," *Rev. Mod. Phys.* **15**, 1 (1943).
 - [13] W.-T. Liao, T. Peters, E.-C. Shen, and I. A. Yu, "Propagation, Broadening, and Energy Decay of Quasi-Stationary Light Pulses in Thermal Atoms," *Chin. J. Phys.* **47**, 043603 (2006).
 - [14] Y.-H. Chen, M.-J. Lee, I.-C. Wang, S. Du, Y.-F. Chen, Y.-C. Chen, and I. A. Yu, "Coherent Optical Memory with High Storage Efficiency and Large Fractional Delay," *Phys. Rev. Lett.* **110**, 083601 (2013).